ADVANCED QUANTUM TECHNOLOGIES
www.advquantumtech.com

Zeptosecond-Scale Single-Photon Gyroscope

Fabrizio Sgobba, Danilo Triggiani, Vincenzo Tamma, Paolo De Natale, Gianluca Gagliardi, Saverio Avino, and Luigi Santamaria Amato**

This work presents an all-fiber telecom-range optical gyroscope employing a spontaneous parametric down conversion crystal to produce ultra-low intensity thermal light by tracing-out one of the heralded photons. The prototype exhibits a detection limit on photon delay measurements of 249 zs over a 72 s averaging time and 26 zs in differential delay measurements at $t = 10^4$ s averaging. The detection scheme proves to be the most resource-efficient possible, saturating > 99.5% of the Cramér–Rao bound. These results are groundbreaking in the context of low-photon regime quantum metrology, paving the way to novel experimental configurations to bridge quantum optics with special or general relativity.

1. Introduction

Fringe interferometry represents the most sensitive tool for optical metrology. The ability to discern tiny variations of interference patterns allows accurate measurements of environmental or sample parameters with a sensitivity scaling as the inverse frequency of the radiation source. Many different geometries, such as Michelson, Fabry–Pérot, Mach–Zehnder or Sagnac schemes to name a few, have been successfully investigated over time and employed in a wide variety of applications including high precision geometry,[1] relativistic testing and gravitational wave detection (as in the LIGO/VIRGO experiments,[2]) spectroscopy[3] as well as accurate real-time ranging.[4]

First demonstrated by Sagnac in 1913,[5] the interferometric technique carrying his name is arguably one of the most robust among all interferometric configurations. Here, a single beam of light is separated into two counter-propagating beams and introduced in a closed loop, that may be arranged in different geometries where the square or circular shape are most common ones.[6] An interference pattern arises whenever the loop undergoes rotation, due to the difference in path-lengths between the two counter-propagating beams. Since both beams travel along the same path, such configuration is intrinsically insensitive to variations in temperature or environmental noise, such as mechanical vibrations, occurring on timescales much larger than the round-trip time (as is usually the case for most environmental noise), thus making it particularly appealing for its intrinsic robustness.

Since the dawn of fiber-optic communication, Sagnac interferometry proved to be naturally suited to be implemented in all fiber-based setups, giving rise to the now widely diffused fibre-optic gyroscope (FOG) interferometry,[7] a competitive alternative to the more complex free-space ring laser gyroscope (RLG),[8] where an active Sagnac interferometer generates two measurable optical beating notes. These techniques became progressively more sensitive and reliable following the technological advances of the recent decades in optical fiber coupling as well as fiber-coupled optical sources and detectors, finding their application in so many different fields,[9] from geodesy to hydrophony and geophony for military and civil applications, to precise ground positioning, that a comprehensive list would become a review on its own (see Refs. [10, 11]) In addition to FOG performances, which are rapidly improving, and to its fields of application, which are ever-expanding;[6] a great deal of effort is being expended to produce increasingly small FOG.[12] On the other hand, the latest advances in single photon detection techniques[13,14] led to a strongly renewed scientific interest toward quantum optics and quantum interferometry beyond more direct application areas such as quantum communication, teleportation, or quantum key distribution. For example, Hong–Ou–Mandel interferometry[15,16] sensing capabilities

F. Sgobba, L. Santamaria Amato
Italian Space Agency (ASI)
Centro Spaziale 'Giuseppe Colombo'
Località Terlecchia, 75100 Matera, Italy
E-mail: luigi.santamaria@asi.it

F. Sgobba, G. Gagliardi, S. Avino, L. Santamaria Amato
Consiglio Nazionale delle Ricerche
Istituto Nazionale di Ottica (INO)
Via Campi Flegrei 34, Comprensorio A.Olivetti, I-80078 Pozzuoli, Italy
E-mail: saverio.avino@ino.cnr.it

D. Triggiani, V. Tamma
School of Mathematics and Physics
University of Portsmouth
Portsmouth PO1 3QL, UK

V. Tamma
Institute of Cosmology and Gravitation
University of Portsmouth
Portsmouth PO1 3FX, UK

P. De Natale
Consiglio Nazionale delle Ricerche
Istituto Nazionale di Ottica (INO)
Largo E. Fermi 6, I-50125 Firenze, Italy

The ORCID identification number(s) for the author(s) of this article can be found under https://doi.org/10.1002/qute.202400166

DOI: 10.1002/qute.202400166

when complemented by Fisher information analysis[17,18] as well as delayed choice quantum erasers[19] led to attosecond-level resolution in delay measurements in low optical intensity regimes, paving the way for noninvasive biosensing and non-perturbing optical metrology. Increasing applications of integrated devices based on Sagnac effect in quantum optics are expected in the near future as development of quantum sources[20] and sensors[21] just to name a few. In a quantum experiment aiming to highlight the interplay and coexistence of general relativistic effects with quantum mechanics, a sharp distinction has to be made between classical behaviors and quantum mechanics-related behaviors, as well as between general relativistic and Newtonian descriptions. If such boundary results more blurred when massive particles are involved,[22] a fully optical experiment involving gravitational effects represents the ideal candidate due to the masslessness of the photon. Hence, the latest results in quantum metrology are reported in Refs. [17, 19] together with challenging experiments adopting similar setups both for test of fundamental physics[23,24] and for more practical applications,[25,26] have fueled a wave of theoretical investigations on quantum-relativistic interface experiments both in free space and in fiber.[27–29]

Brady et al.,[29] e.g., were able to estimate a lower bound on photon delay detection limit (σ) needed for the detection of the Sagnac effect due to Earth's rotation, using an interferometer of total area $\mathcal{A}$, via the figure of merit F, defined as $F = \frac{\sigma}{\mathcal{A}}$. The bound retrieved was $F \sim 10^{-15}$ s km^{-2}, which means that attosecond-level ($\approx 10^{-18}$ s) delay sensing would require a total interferometer area $\mathcal{A} > 1000$ m^2.

This paper presents what is, to the best of our knowledge, the first ultra-low photon regime delay sensor based on a 2 km fiber FOG with quadrupole-winding designed to operate in the telecom region (1550 nm) to minimize attenuation. The combination of highly performing near-infrared single-photon detectors, together with quadrupole-winded FOG interferometry and serrodyne modulation, not employed in other single photon FOG setups,[23,25] led to establish a new limit both on the measurement of the key quantity $F = \frac{\sigma_\tau}{\mathcal{A}} \sim 2 \times 10^{-15}$ s km^{-2}at $t = 72$ s integration time and on the delay detection limit itself, obtaining for the first time an uncertainty as low as 249 zs in 72 sec integration time and 26 zs in differential delay measurements, which, so far, had never been achieved in photon counting regime.

2. Experimental Setup

In the proposed setup the optical source was composed of twin photons source (TPS, panel 1. in **Figure 1**), where a continuous wave (CW) diode laser, centered at 775 nm, pumped a periodically-poled Lithium-Niobate (PPLN) crystal cut for type-II spontaneous parametric down conversion (SPDC), and specifically designed to maximize its down conversion efficiency at the center wavelength of 1550 nm, provided that its temperature was actively stabilized at 33.9° C.

Each correlated photon pair produced by the TPS was then separated via a polarizing beam splitter (PBS, panel 2. in Figure 1), so that it was always possible to select a single photon (having horizontal polarization) from the pair.

The selected photon entered in the fiber-coupled optical circulator from the input port A (see panel 3. in Figure 1).

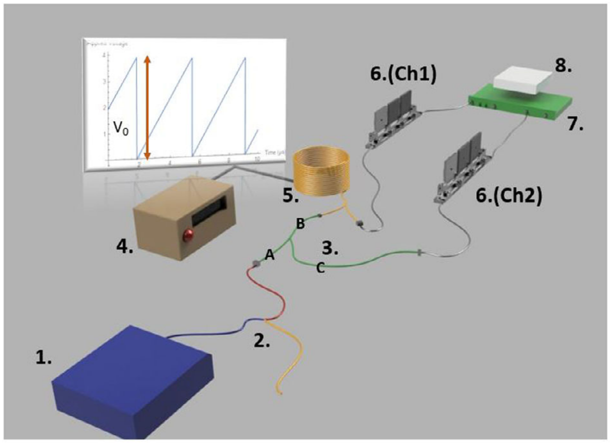

Figure 1. 3D realistic sketch of the employed experimental setup. 1.) Twin photon source, 2.) polarizing beam splitter, 3.) optical circulator, 4.) waveform generator, 5.) gyroscope, 6.) polarization rotation paddles, 7.) Superconductive nanowires single-photon detectors, and 8.) Time tagging electronics.

The circulator allowed light entering from port A to come out of port B, whereas light entering from B to come out of port C. Port B was therefore connected to one of the inputs/outputs of a 2 km-long FOG of total area $\mathcal{A} = 125$ m^2. The FOG presented itself as a fiber spool having average radius of 12.5 cm (refractive index $n = 1.471$) and a total volume of $\approx 6000\ cm^3$. Therefore, the 2 km fiber was wound up into $N \sim 2550$ coils. The interferometer was engineered in such a way that the forward and backward propagating paths underwent as similar environmental conditions as possible. In order to obtain this goal, the coils were wrapped in a quadrupole configuration, that ensured time-dependent temperature and strain variations affect in the same way both propagation directions. Embedded within the spool was a fiber-coupled electro-optical modulator (EOM), tasked to provide a voltage-driven time-dependent phase shift between two propagating directions i.e., serrodyne modulation.[30]

In the serrodyne modulation, the voltage had to be applied via a waveform generator (panel 4. in Figure 1) in the form of a saw-tooth wave having a period equal to twice the round-trip time inside the interferometer. In this specific case, the repetition rate resulted to be $\nu_{ramp} = 54.795$ kHz. In this experimental configuration, the total phase delay $\Delta\phi$ established between counter-propagating paths was directly proportional to the peak–peak voltage applied to the EOM (V_0 with reference to Figure 1).

It was helpful to introduce the parameter $\tau = \frac{\Delta\phi}{\omega_0}$, which corresponded to a relative temporal delay between the counter-propagating paths that would generate the dephasing $\Delta\phi$ at central angular frequency ω_0. τ is, in turn, proportional to the applied voltage V_0. Therefore, it could be expressed as

$$\tau = \alpha V_0 \tag{1}$$

Where the proportionality constant α was introduced, the estimation of which had to be performed by calibration. For example, if a specific applied voltage V_{0i} provides a total dephasing of $\Delta\phi = \frac{\pi}{2}$

for a $\lambda_0 = 1550$ nm photon between forward and backward propagating paths,

$$\tau(V_{0i}) = \frac{\Delta\phi(V_{0i})}{\omega_0} = \frac{\pi}{2\omega_0} = \frac{\lambda_0}{4c} = 1.294\times10^{-15}\ \mathrm{s} = 1.294\ \mathrm{fs} \tag{2}$$

Where c is the speed of light in vacuum. Hence,

$$\alpha = \frac{\tau(V_{0i})}{V_{0i}} = \frac{1.294\times10^{-15}}{V_{0i}}\frac{\mathrm{s}}{\mathrm{V}} \tag{3}$$

One of the two input/outputs of the gyroscope was then connected to the first channel (Ch1) of the detector, consisting in a two-channels array of He-cooled superconducting nanowires single photon detectors (SNSPDs, panel 7. in Figure 1). The second channel (Ch2) was connected to port C of the optical circulator so that light coming from the gyroscope and entering into port B could be collected in Ch2. Since SNSPDs efficiency was strongly dependent on impinging light polarization, each channel was provided with a polarization rotation paddle (panel 6. in Figure 1) in order to rotate the photon polarization to maximize the detectors efficiency.

Both channels were connected to a time-tagging device (panel 8. in Figure 1) for data collection.

3. Theoretical Framework

The pure photon-pair state generated via type-2 SPDC can be written as

$$|\Psi\rangle = \int_{\mathbb{R}} \mathrm{d}\omega\; g(\omega) a^{\dagger}_{\mathrm{H}}(\omega) a^{\dagger}_{\mathrm{V}}(\omega_p - \omega)|0\rangle \tag{4}$$

where ω_p is the pump frequency, $g(\omega)$ is the joint spectral amplitude, and $a^{\dagger}_{\mathrm{H/V}}(\omega)$ denotes the photonic creation operator associated with a photon with frequency ω and polarization H or V. The effect of the polarizing beam splitter, selecting only the photons with vertical polarization, is to trace out from Equation (4) the horizontally polarized photon. The state injected in the FOG is thus mixed and reads

$$\rho = \int_{\mathbb{R}} \mathrm{d}\omega \mathrm{d}\omega'\; \rho(\omega,\omega') a^{\dagger}_{\mathrm{H}}(\omega)|0\rangle\langle 0| a_{\mathrm{H}}(\omega') \tag{5}$$

where

$$\begin{aligned}\rho(\omega,\omega') &= \int_{\mathbb{R}} \mathrm{d}\omega_1 \langle 0| a_{\mathrm{H}}(\omega) a_{\mathrm{V}}(\omega_1)|\Psi\rangle\langle\Psi| a^{\dagger}_{\mathrm{H}}(\omega') a^{\dagger}_{\mathrm{V}}(\omega_1)|0\rangle \\ &= |g(\omega)|^2 \delta(\omega-\omega')\end{aligned} \tag{6}$$

is the matrix representation of ρ.

For all extents, the FOG introduced in the previous section can be treated as a Sagnac interferometer, or a Mach–Zehnder interferometer where input and output beam splitters (BS) coincide, as shown in **Figure 2**

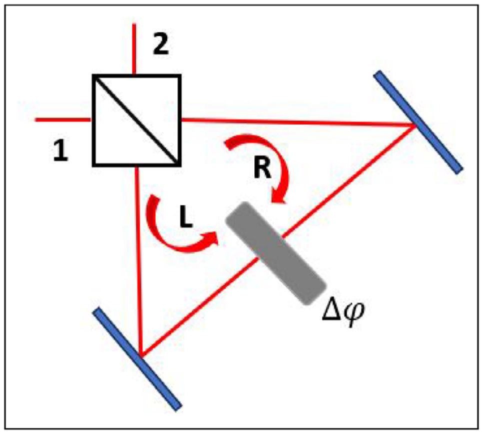

Figure 2. Schematic depiction of a Sagnac interferometer.

In the proposed setup, the photon enters from port 2, with reference to Figure 2. Since, for all practical purposes, the photon polarization state is irrelevant for the remainder of these calculations, for simplicity we will omit the subscript H from Equation (5) and we replace it with a subscript $i = 1, 2, R, L$ indicating, again with reference to Figure 2, the channel in which the photon propagates. The evolution of the operator $a^{\dagger}_2(\omega)$, impinging on the beam splitter and undergoing the phase differential $\Delta\varphi$ first, and then exiting the interferometer, is given by

$$\begin{aligned}&a^{\dagger}_2(\omega) \to \frac{1}{\sqrt{2}}\left(a^{\dagger}_R(\omega)e^{\mathrm{i}\Delta\phi} + a^{\dagger}_L(\omega)\right) \to \\ &\frac{1}{2}\left[a^{\dagger}_2(\omega)\left(e^{\mathrm{i}\Delta\phi}+1\right) + a^{\dagger}_1(\omega)\left(e^{\mathrm{i}\Delta\phi}-1\right)\right].\end{aligned} \tag{7}$$

The state at the output of the interferometer can thus be written as

$$\begin{aligned}\rho_{\mathrm{out}} = \frac{1}{4}\int_{\mathbb{R}} \mathrm{d}\omega |g(\omega)|^2 &\left[a^{\dagger}_2(\omega)\left(e^{\mathrm{i}\Delta\phi}+1\right) + a^{\dagger}_1(\omega)\left(e^{\mathrm{i}\Delta\phi}-1\right)\right] \\ &|0\rangle\langle 0|\left[a_2(\omega)\left(e^{-\mathrm{i}\Delta\phi}+1\right) + a_1(\omega)\left(e^{-\mathrm{i}\Delta\phi}-1\right)\right]\end{aligned} \tag{8}$$

where $\Delta\phi = \omega\tau$ is the relative dephasing between the two counter-propagating paths.

The probabilities to register a click at the first or second channel, respectively P_1 and P_2, can therefore be written as

$$\begin{aligned}P_{2/1} &= \int_{\mathbb{R}} \mathrm{d}\omega\; \langle 0| a_{2/1}(\omega)\rho_{\mathrm{out}} a^{\dagger}_{2/1}(\omega)|0\rangle \\ &= \frac{1}{2}\left(1 \pm \int_{\mathbb{R}} \mathrm{d}\omega\; |g(\omega)|^2 \cos(\omega\tau)\right)\end{aligned} \tag{9}$$

For a photon having a Gaussian spectral distribution with a linewidth σ_ω and a center angular frequency ω_0, described by a normalized spectral distribution

$$|g(\omega)|^2 = \frac{1}{\sqrt{2\pi\sigma^2_\omega}} e^{-\frac{(\omega-\omega_0)^2}{2\sigma^2_\omega}} \tag{10}$$

the probability distribution reads

$$P_{2/1} = \frac{1}{2}\left(1 \pm e^{-\frac{\sigma^2_\omega \tau^2}{2}} \cos(\omega_0\tau)\right) \tag{11}$$

From Equation (11), it follows that by measuring the counts events on each channel (which are proportional to the outcome probability $P_{1/2}$ once the dark counts are removed), it is possible to retrieve the value of the delay τ between propagating and counter-propagating probability amplitudes, and ultimately to retrieve the rotational angular velocity Ω of the reference frame to which the Sagnac interferometer is bound. In order to obtain the most sensitive possible experimental condition for the measurement of the parameter τ it results mandatory to evaluate the Fisher information, namely the variance of the score (defined as the gradient of the logarithm of the likelihood function).[17,31,32] As extensively discussed in Ref. [31] given a parameter θ conditioning the measurement outcomes $m \in M$ with a probability distribution $P(m|\theta)$, which expresses the probability of outcome m given θ, the Fisher information is defined as

$$\mathcal{F}(\theta) = \sum_{m \in M} \frac{1}{P(m|\theta)} \left(\frac{\partial}{\partial \theta} P(m|\theta) \right)^2 \tag{12}$$

The importance of the Fisher information resides in the fact that it yields the maximum precision achievable in the unbiased estimation of τ with a given measurement scheme through the Cramér–Rao bound[33]

$$\sigma_\tau(N) \geqslant \frac{1}{\sqrt{N\mathcal{F}(\tau)}} \tag{13}$$

where $\sigma_\tau(N)$ is the uncertainty associated with the estimation, and N is the number of repetitions of the experiment, namely the total number of detected photons. Hence, larger values of the Fisher information yield better sensitivities.

Once the Fisher information and the number of detected photons have been determined, the degree of saturation of the Cramér–Rao bound (i.e. the quantity $S(\tau) = (\sqrt{N\mathcal{F}(\tau)}\sigma_\tau(N))^{-1}$, $S \leq 1$) is a powerful metric to determine how efficiently the experimental setup is capable to extract information by each one of the detected photons. A fully saturated ($S(\tau) = 1$) Cramér–Rao bound therefore qualifies the experimental procedure as the most efficient to estimate the chosen parameter, all other experimental conditions being equal.

The partial derivative squared of the probability function $P_{2/1}$ with respect to the conditioning parameter τ follows from Equation (11) as

$$\begin{aligned}(\partial P_{2/1})^2 &= \frac{1}{4}\left(\mp \frac{\sigma_\omega^2}{2} \tau e^{-\frac{\sigma_\omega^2 \tau^2}{2}} \cos(\omega_0 \tau) \mp \frac{\omega_0}{2} e^{-\frac{\sigma_\omega^2 \tau^2}{2}} \sin(\omega_0 \tau) \right)^2 \\ &= \frac{1}{4} e^{-\sigma_\omega^2 \tau^2} \left(\sigma_\omega^2 \tau \cos(\omega_0 \tau) + \omega_0 \sin(\omega_0 \tau) \right)^2 \end{aligned} \tag{14}$$

The Fisher information of this system, as a function of the parameter τ, reads therefore

$$\mathcal{F}(\tau) = e^{-\sigma_\omega^2 \tau^2} \frac{\left(\sigma_\omega^2 \tau \cos(\omega_0 \tau) + \omega_0 \sin(\omega_0 \tau) \right)^2}{1 - e^{-\sigma_\omega^2 \tau^2} \cos^2(\omega_0 \tau)} \tag{15}$$

The linewidth of the SPDC source employed results to be $\sigma_\omega \approx 0.25$ THz, whereas $\omega_0 = 2\pi\nu_0 \approx 1.21 \times 10^3$ THz. The Fisher information evaluated for a delay varying in the range $\tau \in [0, 5000 \text{ fs}]$ is reported in **Figure 3**.

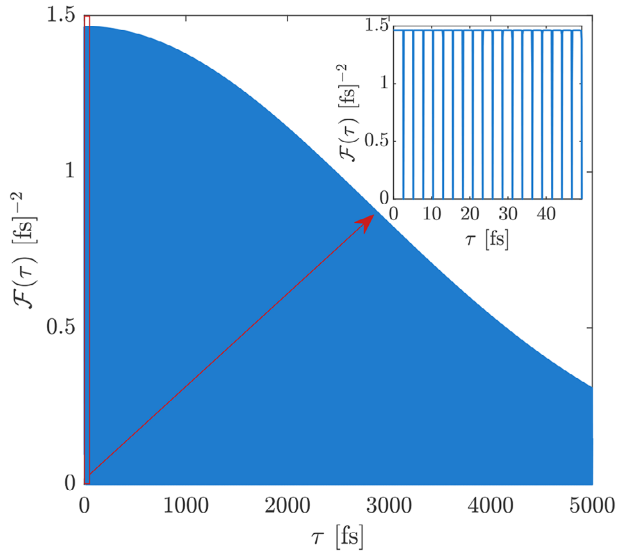

Figure 3. Simulation of the Fisher information $\mathcal{F}(\tau)$ for the system reported in Figure 1, the inset shows $\mathcal{F}(\tau)$ in the first 50 fs.

In low delays regime, where $\sigma_\omega \tau \ll 1$ and $\sigma_\omega^2 \tau \ll \omega_0$, Equation (15) becomes

$$\mathcal{F}(\tau) \approx \omega_0^2 \tag{16}$$

everywhere except for $\omega_0 \tau = (2l + 1)\pi$, $l \in \mathbb{N}$.

4. Results and Discussion

4.1. Gyroscope Characterization and Sensor Calibration

In order to determine precisely the inflection point for the probabilities in Equation (11), where $\Delta\phi_i = \frac{\pi}{2}$, we decided to operate in high-intensity regime and we replaced the twin photon source with a superluminescent light emitting diode (SLED) filtered at 1550 nm with a bandwidth of 1 nm. The output power has been then measured as a function of the voltage V_0 applied to the waveform generator by means of an optical power meter. Acquired data have been plotted and fitted with a sine function

$$f_{fit}(V_0) = f_0 + A \sin\left(\pi \frac{V_0 - V_{0i}}{w} \right) \tag{17}$$

for both gyroscope outputs (see **Figure 4**).

The values of the parameters A, w, f_0, V_{0i} have been extracted from the plot in Figure 4 and summarized in **Table 1** with their respective fit errors. From these, the final value for the inflection point has been retrieved via weighted average as

$$< V_{0i} >= 3.8596 \pm 0.0095 \text{ V} \tag{18}$$

Consequently, the proportionality constant α results

$$\alpha = (3.35 \pm 0.03) \times 10^{-16} \frac{\text{s}}{\text{V}} \tag{19}$$

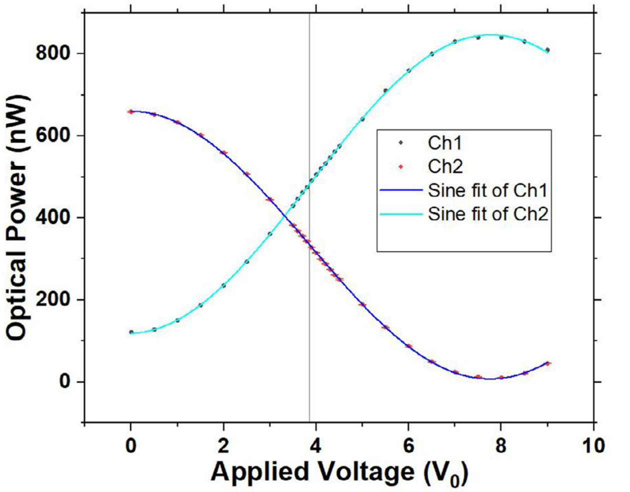

Figure 4. Optical power output of the FOG while employing a filtered incoherent bright source for Ch1 (in black) and Ch2 (in red), measured at a fixed applied Voltage (V). A reference line is reported for $V_0 = 3.8596$ V. The fits of Ch1 and Ch2 with the function $f_{fit}(V_0)$ are reported as blue and cyan lines respectively.

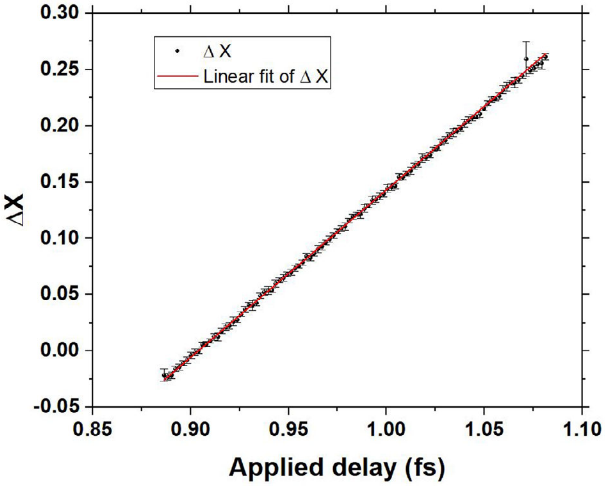

Figure 5. The experimental values of $\Delta X = X_1 - X_2$, and the corresponding applied delays τ at which have been retrieved, fitted with a linear calibration curve.

It can be observed how, if the half-period w results comparable within the fit error, the amplitude A and the offset f_0 differ between the channels. The $\approx$ 10% discrepancy in amplitude has to be traced back to unbalanced losses in the channels that cannot be attributed to the FOG or to the particular detector employed (since the output power on both channels for the bright-source setup has been measured with the same optical power meter), but arguably depends on the fibers and on the circulator. The residual offset on Ch1, $f_0 - A \sim 120$ nW, can be attributed to back-reflections happening before the EOM and affecting the output connected to Ch1 itself as well as to non perfect visibility. Residual offset on Ch2 results instead comparable to the background noise seen by the power meter.

Figure 4 shows, that for an applied voltage V_0 comprised between the values of 3.6 and 4.4 V, both channels show linearity between applied voltage and optical power. Hence, this region results to be the best candidate to perform a calibration of the delay sensor.

The actual delay sensor calibration and the subsequent measurements have been therefore performed with the single photon setup shown in Figure 1.

For $V_0 \in [3.6\ , 4.4\ \text{V}]$, each value of the applied voltage V_0 (and consequently delay τ) will return a value of single count events on each channel ($C_{1/2}$) linearly dependent on V_0.

The introduction of

$$X_1 = \frac{C_1}{C_1 + C_2} \qquad X_2 = \frac{C_2}{C_1 + C_2} \tag{20}$$

allows to renormalize the single count events by the sum of all tagged counts in order to rule out fluctuations coming from the optical pump. The calibration curve can be written as ($\Delta X = X_1 - X_2$)

$$\Delta X = K_1 \tau + K_2 \tag{21}$$

To reduce the amount of dark count events, both the calibration and the measurements reported in the following sections have been performed after sunset. In these conditions, each channel experienced stable dark counts of $dc \sim 20 - 30$ Hz, close to electronics-related dark counts ($\approx 10 - 20$ Hz) and negligible with respect to the signal on each channel during the measurement ($C_1 \approx C_2 \sim 300 - 350$ kHz).

The calibration routine consisted in 100 steps between the values of $V_{0a} = 3.6$ V and $V_{0b} = 4.4$ V. Each step has been acquired ten times with an acquisition time of 100 ms in order to retrieve, for each step, an average value of $(X_1, X_2, \Delta X)$ and an error, evaluated propagating the error resulting from the standard deviation on $C_{1/2}$ of the ten acquisitions per step.

The calibration of the delay sensor is reported in **Figure 5**, and the retrieved calibration parameters K_1, K_2 are reported in **Table 2**.

4.2. Long-Term Measurement

Right after the calibration we performed a 9 h-long acquisition over night, using an integration time of $T = 1$ s per point. The function generator commands were set to provide a sawtooth wave of peak-to-peak amplitude $V_0 = 3.86$ V.

Table 1. Parameters retrieved from fit.

Channel	V_{0i} [V]	w [V]	A [nW]	f_0 [nW]
Ch1	3.85 ± 0.01	7.84 ± 0.04	364 ± 1	482 ± 1
Ch2	3.93 ± 0.03	7.79 ± 0.03	327 ± 1	334 ± 1

Table 2. Parameters retrieved from calibration.

K_1 [fs^{-1}]	K_2
1.0937 ± 0.0036	-1.3432 ± 0.0049

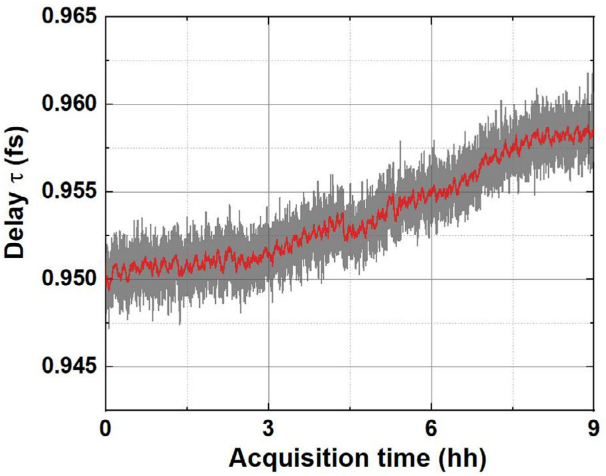

Figure 6. Long term acquisition with acquisition time expressed in hours (hh), $T = 1$ s integration time, $V_0 = 3.86$ V applied voltage. In red, the same data smoothed by adjacent average at 72 s integration time.

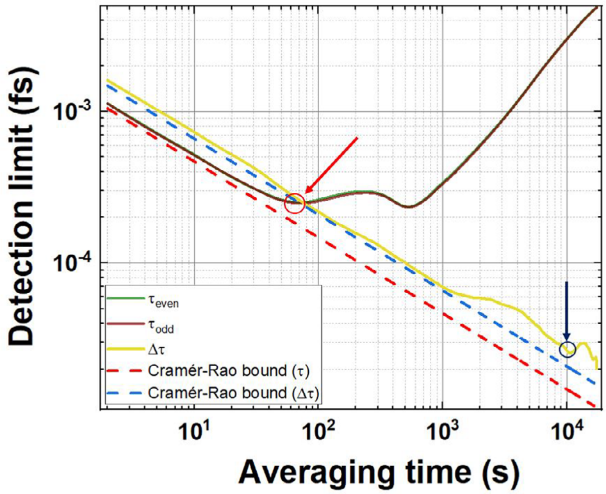

Figure 7. OAdev analysis of the long term measurement reported in Figure 6, sliced into even datapoints (in olive green), odd datapoints (in wine) and the deviation of their difference (in yellow). The red and blues dashed lines represent the Cramér–Rao bounds for the detection of τ and $\Delta\tau$, respectively, as a function of the averaging time, proportional to the detected photons. Red and blue arrows and circles highlight the detection limit for τ at 72 s and $\Delta\tau$ at 10^4 s.

A Python script was used to convert acquired single count events on each channel into delays τ by means of Equation (21), employing the values of K_1, K_2 reported in Table 2. The whole acquisition is reported in **Figure 6**.

As can be observed from Figure 6, the system experiences a long-term drift of ≈ 10 as over 9 h. Such drift can be associated to variations in temperature, affecting in particular the EOM piezoactuator embedded within the gyroscope.

In the medium-short term (< 10 min) the instabilities of the pump are still recognizable, even after the renormalization.

A time-domain frequency stability analysis allows both to assess the detection limit that the proposed delay sensor is capable to achieve at different integration times as well as to effectively investigate the different contributions to the noise affecting the signal. It is worth pointing out that, in this case, the detection limit (DL) of the sensor is intended as the measured time delay that can be achieved with a unitary signal to noise ratio (SNR), hence $DL(t) = \sigma(t)$.

For this reason, we performed an overlapping Allan (OA) deviation analysis of the long-term measurement reported in Figure 6, where, given a set of N datapoints $\{x_1, \dots x_N\}$ acquired at integration time t_0, the OA variance at a given time ($t = mt_0$) is defined as[34]

$$\sigma^2_{OA,x}(t) = \frac{1}{2m^2(N-2m+1)} \sum_{j=1}^{N-2m+1} \left(\sum_{i=j}^{j+m-1} x_{i+m} - x_i \right)^2 \tag{22}$$

Several quantum metrology applications[17,19,32] perform differential measurements on their conditioning parameter (in this case, τ) to achieve better long-term stability performances. To allow a more straightforward comparison with such literature, we decided to slice the data acquired and perform the OAdev analysis to even and odd data points separately (retrieving detection limits for τ_{even} and τ_{odd}, respectively), de facto obtaining a $\Delta\tau = 0$ differential measurement that represents the ultimate detection level achievable, once all noise sources (both coming from the source and the environment) are ruled out. The analysis has been plotted and reported in **Figure 7**.

The average count rate of both channels combined during the long term measurement (R) reported in Figure 6 corresponded to $R = 631.6$ kHz. Therefore, since the $\tau_{even/odd}$ values are updated once every 2s, the theoretical Cramér–Rao bound $CRB(\tau)$ derived from Equation (15) becomes (red dashed line in Figure 7)

$$\sqrt{\frac{1}{\mathcal{F}N}} \approx \sqrt{\frac{2}{\omega_0^2 Rt}} \tag{23}$$

For $t < 60$ s, i.e. before medium term oscillations and long term drifts, the proposed system proves to saturate up to 93 − 95% of the Cramér–Rao bound. In particular, from the OA deviation analysis in Figure 7 emerges that the detection limit on τ (red circle) is achieved for $t_{DL} = 72$ s, in correspondence of which the best value is

$$\sigma_{DL} = 2.49 \times 10^{-19} \text{ s} = 249\text{zs} \tag{24}$$

Medium-term oscillations related to the instability of the pump make the OA deviation to increase for $t > 80$ s. As expected from $t \sim 600$ s the OA deviation for the single τ experiences the aforementioned long term drift, which is caused by temperature variations affecting both fibers and EOM response.

The differential detection ($\Delta\tau$), which is unaffected by pump instability or drifts, shows a saturation $S(\Delta\tau) > 99.5\%$ for averaging times $t \sim 10^2 - 10^3$ s. Moreover, at $t = 10^4$ s (blue circle), the total detection limit for differential measurements results

$$\sigma_{\Delta\tau} \approx 26 \text{ zs} \tag{25}$$

5. Conclusion

In this paper, we implemented high-resolution single photon Sagnac interferometry in a 2 km long single mode, polarization maintaining FOG with a quadrupole winding geometry.

Our quantum-based delay sensor, operating in the telecom region and entirely fiber-coupled, shows the best sensitivity performances ever reported in literature for low photons regime Sagnac interferometry, capable to detect delays as low as 249 zs at 72 s integration time, and outperforming similar quantum sensors by more than an order of magnitude.[17,19] The proposed experimental procedure proved to be the most resource-efficient way possible to measure a delay harnessing single photon quantum probability with a Sagnac interferometer since the differential measure $\Delta\tau$ is capable to achieve a Cramér–Rao bound saturation $S > 99.5\%$ for integration times $t > 10^2$s, and sensitivities as low as 26 zs at averaging times $t = 10^4$ s, corresponding to a detection limit on τ of $26/\sqrt{2} \approx 18$ zs in a set-up free from pump noise and drift. The detection limit of 26 zs corresponds to a bias instability of a classical FOG operated with intense light of $\approx 0.96°h^{-1}$ proper of an intermediate grade FOG. Since the employed FOG presents a total area of 125 m^2, the aforementioned drift-free sensitivity at $t = 10^4$ s corresponds to a figure of merit $F = \frac{\sigma_\tau}{A} \sim 1.4 \times 10^{-16}$ s km^{-2}. To fully appreciate the breadth of these results it is helpful to recall that Brady et al.[29] estimated an upper bound on the detection limit per unit area $F \sim 10^{-15}$ s km^{-2} for the detection of Sagnac effect due to Earth rotation.

Hence, provided that the whole setup is mounted on an appositely designed platform capable to tilt by a certain angle (similar to the one proposed in Refs. [23, 35] it will be possible to perform tests based on Sagnac effect due to earth rotation in single photon regime.

Corresponds to a bias instability

Acknowledgements

V. T. acknowledges support from the Air Force Office of Scientific Research (FA8655-23-1-7046). The authors wish to acknowledge Vincenzo Buompane and Graziano Spinelli for technical support.

Agenzia Spaziale Italiana, Nonlinear Interferometry at Heisenberg Limit (NIHL) project (CUP F89J21027890005); This project has received funding from the European Defense Fund (EDF) under grant agreement EDF-2021-DIS-RDIS-ADEQAUDE (n°101103417). Funded by the European Union. Views and opinions expressed are however those of the author(s) only and do not necessarily reflect those of the European Union. Neither the European Union nor the granting authority can be held responsible for them; PON Ricerca e Innovazione 2014-2020 FESR FSC (Project ARS01 00734 QUANCOM).

Conflict of Interest

The authors declare no conflicts of interest

Data availability statement

The data that support the findings of this study are available from the corresponding author upon reasonable request.

Keywords

Cramér–Rao bound, fibre-optic gyroscope, single photon interferometry

Received: April 11, 2024
Revised: June 10, 2024
Published online: July 8, 2024

[1] S. Yang, G. Zhang, *Meas. Sci. Technol.* **2018**, *29*, 102001.
[2] B. Abbott, R. Abbott, T. Abbott, M. Abernathy, F. Acernese, K. Ackley, C. Adams, T. Adams, P. Addesso, R. Adhikari, V. Adya, C. Affeldt, M. Agathos, K. Agatsuma, N. Aggarwal, O. Aguiar, L. Aiello, A. Ain, P. Ajith, B. Allen, A. Allocca, P. Altin, S. Anderson, W. Anderson, K. Arai, M. Arain, M. Araya, C. Arceneaux, J. Areeda, N. Arnaud, *Phys. Rev. Lett.* **2016**, *116*, 061102.
[3] N. Hoghooghi, R. J. Wright, A. S. Makowiecki, W. C. Swann, E. M. Waxman, I. Coddington, G. B. Rieker, *Optica* **2019**, *6*, 28.
[4] I. Coddington, W. C. Swann, L. Nenadovic, N. R. Newbury, *Nat. Photonics* **2009**, *3*, 351.
[5] G. Sagnac, *CR Acad. Sci.* **1913**, *157*, 708.
[6] H. Arianfard, S. Juodkazis, D. J. Moss, J. Wu, *Appl. Phys. Rev.* **2023**, *10*, 1.
[7] H. C. Lefèvre, *C. R. Phys.* **2014**, *15*, 851.
[8] W. W. Chow, J. Gea-Banacloche, L. M. Pedrotti, V. E. Sanders, W. Schleich, M. O. Scully, *Rev. Mod. Phys.* **1985**, *57*, 61.
[9] B. Culshaw, *Opt. Photonics News* **2005**, *16*, 24.
[10] B. Culshaw, *Meas. Sci. Technol.* **2005**, *17*, R1.
[11] H. Lefevre, *Gyroscopy Navig.* **2012**, *3*, 223.
[12] F. Dell'Olio, T. Natale, Y.-C. Wang, Y.-J. Hung, *IEEE Sens. J.* **2023**, *23*, 29948.
[13] R. H. Hadfield, J. Leach, F. Fleming, D. J. Paul, C. H. Tan, J. S. Ng, R. K. Henderson, G. S. Buller, *Optica* **2023**, *10*, 1124.
[14] S. Dello Russo, A. Elefante, D. Dequal, D. K. Pallotti, L. Santamaria Amato, F. Sgobba, M. Siciliani de Cumis, *Photonics* **2022**, *9*, 470.
[15] D. Branning, A. L. Migdall, A. Sergienko, *Phys. Rev. A* **2000**, *62*, 063808.
[16] E. Dauler, G. Jaeger, A. Muller, A. Migdall, A. Sergienko, *J. Res. National Inst. Stand. Technol.* **1999**, *104*, 1.
[17] A. Lyons, G. C. Knee, E. Bolduc, T. Roger, J. Leach, E. M. Gauger, D. Faccio, *Sci. Adv.* **2018**, *4*, 5.
[18] D. Triggiani, G. Psaroudis, V. Tamma, *Phys. Rev. Appl.* **2023**, *19*, 044068.
[19] F. Sgobba, A. Andrisani, S. Dello Russo, M. Siciliani de Cumis, L. Santamaria Amato, *Sensors* **2023**, *23*, 7758.
[20] J. Park, H. Kim, H. S. Moon, *Phys. Rev. Lett.* **2019**, *122*, 14.
[21] M. R. Grace, C. N. Gagatsos, Q. Zhuang, S. Guha, *Phys. Rev. Applied* **2020**, *14*, 3.
[22] M. Zych, F. Costa, I. Pikovski, T. C. Ralph, Č. Brukner, *Classical Quantum Gravity* **2012**, *29*, 224010.
[23] S. Restuccia, M. Toroš, G. M. Gibson, H. Ulbricht, D. Faccio, M. J. Padgett, *Phys. Rev. Lett.* **2019**, *123*, 11.
[24] G. Bertocchi, O. Alibart, D. B. Ostrowsky, S. Tanzilli, P. Baldi, *J. Phys. B: At., Mol. Opt. Phys.* **2006**, *39*, 1011.
[25] M. Fink, F. Steinlechner, J. Handsteiner, J. P. Dowling, T. Scheidl, R. Ursin, *New J. Phys.* **2019**, *21*, 053010.
[26] C. Zhou, G. Wu, L. Ding, H. Zeng, *Appl. Phys. Lett.* **2003**, *83*, 15.
[27] D. Rideout, T. Jennewein, G. Amelino-Camelia, T. F. Demarie, B. L. Higgins, A. Kempf, A. Kent, R. Laflamme, X. Ma, R. B. Mann, E. Martín-Martínez, N. C. Menicucci, J. Moffat, C. Simon, R. Sorkin, L. Smolin, D. R. Terno, *Classical Quat. Grav.* **2012**, *29*, 224011.

[28] C. Hilweg, F. Massa, D. Martynov, N. Mavalvala, P. T. Chruściel, P. Walther, *New J. Phys.* **2017**, *19*, 033028.
[29] A. J. Brady, S. Haldar, *Phys. Rev. Res.* **2021**, *3*, 2.
[30] H. C. Lefevre, *The Fiber-optic Gyroscope*, 3rd ed., Artech House, USA **2014**.
[31] S. M. Kay, *Prentice Hall* **1993**, Prentice hall, Hoboken, New Jersey, Ch.1.
[32] N. Harnchaiwat, F. Zhu, N. Westerberg, E. Gauger, J. Leach, *Opt. Express* **2020**, *28*, 2210.
[33] H. Cramér, *Mathematical methods of statistics*, volume *9*, Princeton university press, New Jersey **1999**.
[34] D. A. Howe, D. B. Sullivan, D. W. Allan, F. L. Walls, *Characterization of clocks and oscillators NIST Technical Note 1337*, National Institute of Standards and Technology, USA **1990**.
[35] M. Fink, A. Rodriguez-Aramendia, J. Handsteiner, A. Ziarkash, F. Steinlechner, T. Scheidl, I. Fuentes, J. Pienaar, T. C. Ralph, R. Ursin, *Nat. Commun.* **2017**, *8*, 1.